X-31A VECTOR High Angle of Attack Descent Euler and Navier-Stokes Simulations of Unsteady Manoeuvres

Stephan M. Hitzel, Edwin van der Weide, Udo Tremel, Herbert Rieger
Numerical Flow Simulation, EADS Military Aircraft, Munich, Germany

Abstract

The X-31A VECTOR high angle of attack descent manoeuvre is performed in close proximity to the ground and controlled by the application of conventional controls together with a thrust vectoring system. Selected conditions of these manoeuvres were chosen for steady Navier-Stokes simulations in unstructured hybrid computational grids. Unsteady motions of the aircraft and the thrust vector system were performed in Euler-simulations to save on the computational effort due to the neglect of viscous effects. Some aspects of the unstructured grid generation will be discussed. The DLR-TAU code was used as Navier-Stokes solver on multiprocessor machines. The unsteady simulations were performed with the AIRPLANE+-code in the framework of a simulation control tool. Here, this tool guides the aircraft configuration through the flight path evaluated from flight simulation tests.

1 X-31A VECTOR High Angle of Attack Descent Manoeuvre

Past X-31A programs probed the high angle of attack flight well into the post stall regime. The aircraft's sophisticated flight control integrated a 3-D vector nozzle into the canard configuration, which made the manoeuverability of the research aircraft unchallenged. Currently very steep descent flights are prepared to allow for extremely short landings. The highly dynamic manoeuvre is performed in close proximity to the ground and uses the X-31A thrust vector devices to control the aircraft during the descent. The aircraft's slats, flaps and foreplane control a complex system of vortices emanating from the leading edges of the wing, the slats, strakes and the canard (fig. 1).

The flight physical preparations of the VECTOR descent manoeuvres are supported by flow and flight simulations together with investigations into the flow structure and the corresponding pressure distributions and aerodynamic loads.
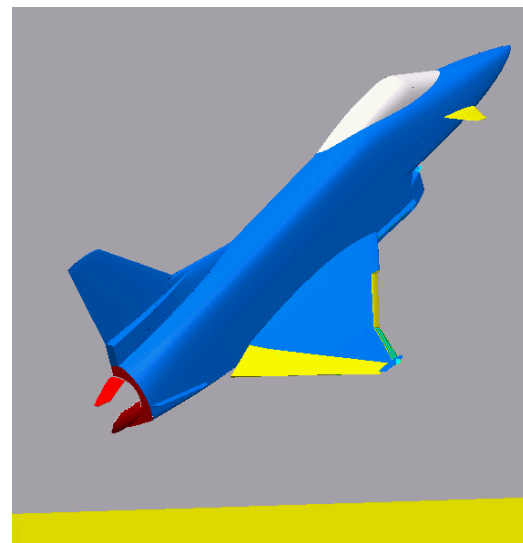

Fig. 1: The X-31A configured for a steep descent manoeuvre close to the ground

2 Numerical Simulation of the Steep Descent Manoeuvre

Out of the steep descent manoeuvre selected positions of the aircraft together with the control settings were chosen for steady state Navier-Stokes simulations. The positions correspond to flight situations. This includes the correct application of the slats and the flaps on the wing, the foreplane angle of incidence and the thrust vectoring devices (figs. 2, 3, 4). Also the engine thrust was simulated according to the engine deck data.

The same positions were compared with and without ground proximity to extract the aerodynamic ground effects for the steady flight conditions of the aircraft and all it's components such as wing, foreplane, slat, flap, fuselage and vector nozzle.
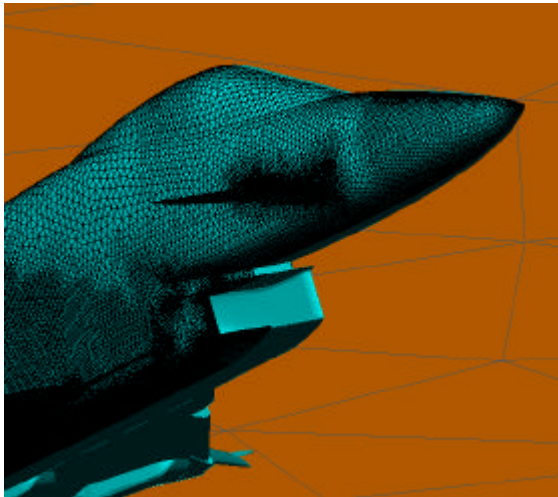
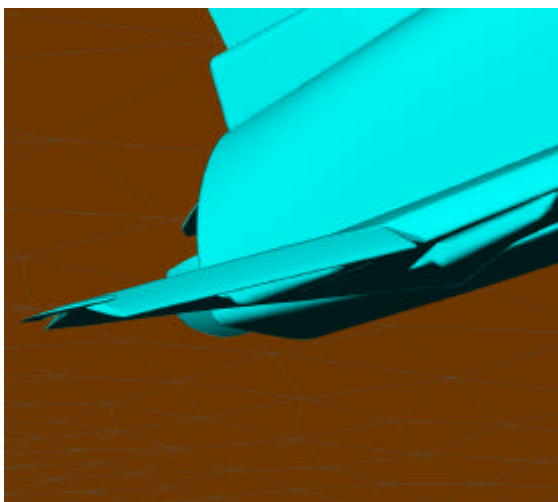Fig. 2: X-31A air-intake, applied foreplane, deployed slats
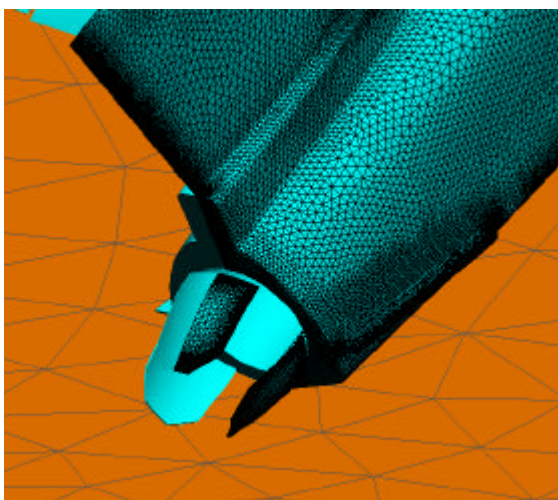

Fig. 3: X-31A deployed slats and flaps

Fig. 4: X-31A thrust vectoring devices and tail

To facilitate the gridding for the simulations the computational domain of the various configurations was discretized with unstructured meshes. For the Navier-Stokes simulations hybrid meshes (fig. 5) with prisms close to the surfaces were utilised while the unsteady Euler simulations were performed in tetrahedral meshes only to save on the complexity and the computational effort due to the neglect of viscous effects.
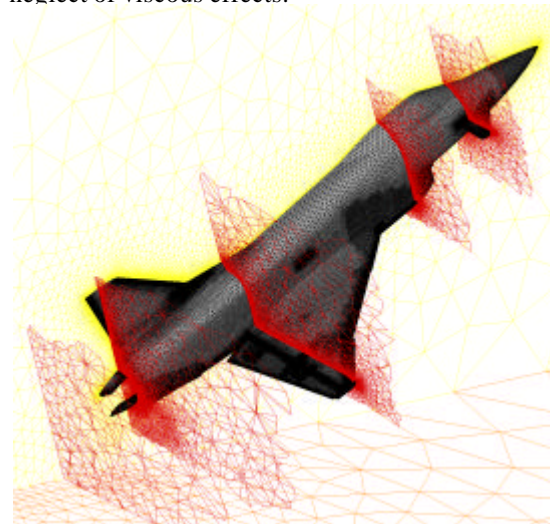

Fig. 5: Hybrid grid of the X-31A configuration

The DLR-TAU code [1] was used as steady state Reynolds-averaged Navier-Stokes solver in partitions well up to 256 processors to allow for reasonable turn around times on nowadays multiprocessor machines. To accelerate the convergence the computations applied the multi-grid agglomeration strategy, which was performed automatically across the multi-processor simulation. To account for the flow turbulence the Spalart-Allmaras model [2] was used.

The Navier-Stokes simulations also were meant to support and verify the unsteady Euler simulations of the manoeuvres and the Euler simulation of applied thrust vector devices. Unfortunately the descent manoeuvre simulation can not be shown here due to delays by more urgent programs.

The manoeuvres were performed in the framework of a simulation control tool together with the AIRPLANE+-code [3]. The AIRPLANE+-code is equipped with a multigrid agglomeration strategy, very similar to the viscous method.

The tools of a simulation control system [4] were employed in guiding the aircraft configuration through the flight path evaluated from flight simulation tests. The aircraft together with it's computational domain is "moved" in the Lagrangian mode in the fixed geodetic frame of reference. The forces and moments on the aircraft and it's components are evaluated in the aircraft and component frame of reference. In this

simulation the aerodynamic control elements were not applied.

The Euler simulation also was employed to perform the effect of moving thrust vector devices relative to the aircraft. Since the vector nozzle components can be modelled as free, independent geometric elements, the numerical grid can be modified by mere motions of the numerical grid leaving it's topology unchanged with relative ease. In a limited way this also holds for small motions of the foreplane surfaces. Larger motions of the latter and the application of slats and flaps would require a re-meshing process on a changing geometric model of the aircraft. The means and methods for such processes are currently under development.

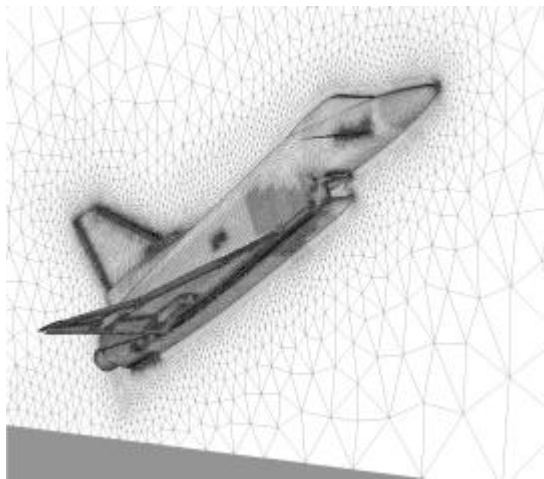## 3 Configuration and Mesh Generation

Fig. 6: Surface grid of the X-31A configuration

To facilitate the meshing of the complex configurations (fig. 1) the unstructured gridding approach (fig. 6) was preferred. Structured meshes would have required the intense interactive build-up of a block structured topology which would have not allowed for small details of slats, flaps or thrust vectoring devices etc. on economic terms such as reasonable multi-grid capable block-sizes and smooth mesh-characteristics close to the configuration.

The "real" non-generic geometry of all configurations was performed in the CATIA 4.3 environment. The collection of the geometry from numerous CAD-models called for intense preparations. A reliable X-31A geometry including the control kinematics, allowing for a fast turn around of different control settings and to meet the challenging demands of mesh-generators was the result.

Since the type of unstructured grid generator used here, supplied by CENTAURSOFT [5] begins meshing with the surface-mesh by a surface-patch based advancing front technique a "water-tight" representation of the geometry is required. Overlaps and gaps had to be closed beforehand.

Since the surface-gridding is restricted to local surface-patches, very elongated and highly pointed triangular surface-elements should be avoided making a rework of a CAD-model inevitable.

An inter-surface-patch gridding technique e.g. utilizing a projection technique applied directly on groups of NURBS surfaces would ease most the problems.

The IGES-input of curve- and surface-NURBS and their transformation into Ferguson-representations called for special care of the distribution of the NURBS-knots to avoid distorted griding on complex surface entities. Those surface-patches have to be transformed by CAD-means and sometimes re-built on other surface types utilizing reworked trimmings. The tightly gridded spot on the side of the centre fuselage of the aircraft in figure 6 shows a harmless example of such a surface-patch. Sometimes this may end in a very bad local mesh quality.

The build-up of the volume grid generally is of reasonable quality, especially when it comes to the introduction of the "Navier-Stokes-prism"-layers once the proper prism parameters are set within a model-suited range. Some experience was required to allow for a good mesh on a low number of passes.

To increase the mesh-resolution around geometric features like wing-edges, intakes etc. and in flow-field regions where important flow features such as vortices or shocks are expected (fig. 7) the definition of source areas for a locally refined gridding were used.
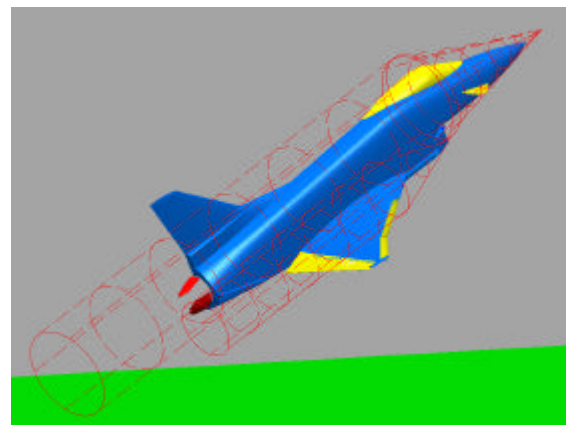

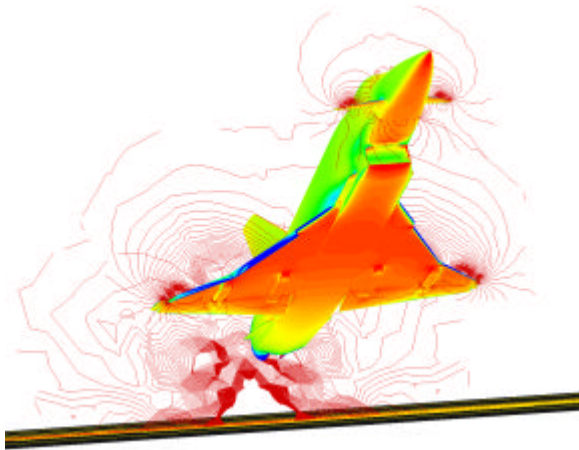Fig. 7: Geometric sources for the X-31A grid

Fig. 8: X-31 A approaching the runway
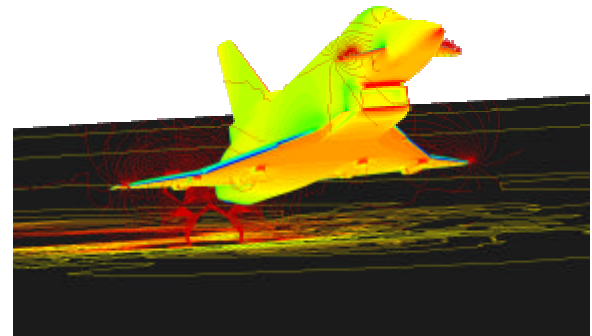(pressure distribution) Case I

Fig. 9: X-31 A close to the end of the steep
descent manoeuvre (pressure distribution) Case II

5 The Flow and it's Structure at the Steep Descent Manoeuvre

Two "key" flight conditions have been selected from a typical steep descent manoeuvre. The figures 8 and 9 show two positions of the X-31A during a steep descent run. The first (Case I) at almost $\alpha = 28^0$ the second (Case II) close to $\alpha = 15^0$, both at low speed (Mach ~ 0.15). In figure 8 the distance of the vector nozzle of the ground is h/b = 0.5, in the other case at h/b = 0.3, where b is the span of the aircraft. For the first case the slats are set at 40^0 inboard and 32^0 outboard, the flaps at $+ 11^0$. while the foreplane is set at $–20^0$. Figure 9 shows the settings for the foreplane and the flaps at almost 0^0, while the slats are applied at 16^0 inboard and at 13^0 outboard.

wing surface shows the effects of a leading-edge vortex system emanating at the inboard and outboard panel of the wing. Also weaker vortices can be found at the foreplane, while the wing-apex strake vortex can be found in the low pressure plot along the lower fuselage just ahead of the wing.
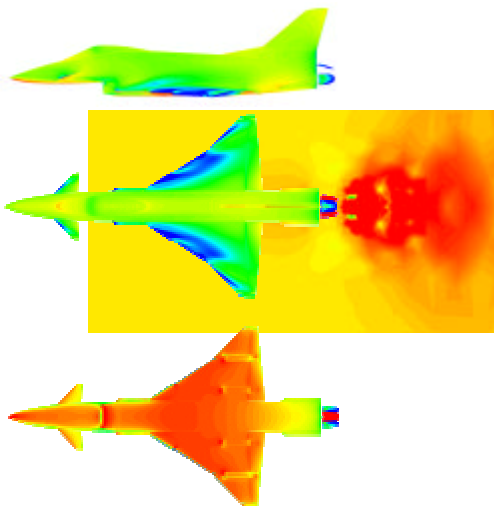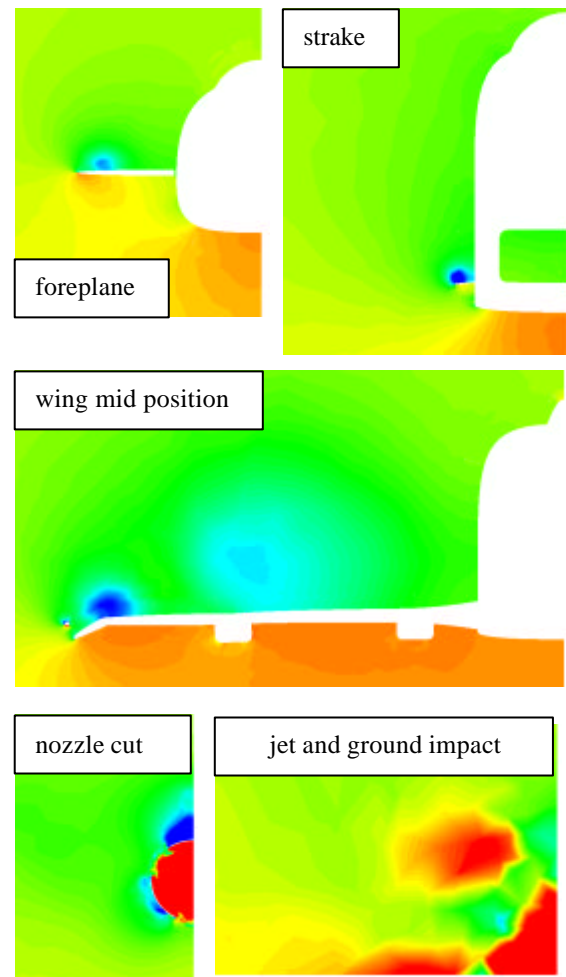

Fig. 10: Pressure distribution on the X-31 A and
pressure imprint onto the runway (Case I)

Figure 10 shows the pressure distribution on the side-, top- and bottom-view of the aircraft as well as the pressure on the runway showing the impinging jet together with the much weaker pressure cushion of the aircraft of Case I. The upper

Fig. 11: Pressure field around the X-31A for Case I

Since the foreplane setting causes a local angle of attack close to 8^0, figure 11 shows a small leading-edge vortex only. The low sweep of the foreplane surfaces triggers an unstable vortex which already has burst at the strake position where a very intense and highly stable vortex system is starting to influence the onset of the wing leading-edge flow. The "wing mid position" cut reveals two major vortices inboard and outboard of the wing. The inner one already shows a large diameter of influence together with a relative high centre pressure indicating some decay - possibly inflicted by the onset of vortex breakdown – of the inboard vortex. The outboard vortex very much benefits from the slat setting, which together with the induced side-wash flow field of the inboard vortex causes a relative stable vortex exhibited by a low pressure in it's core.
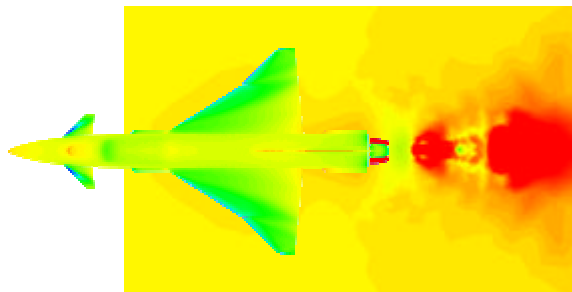

Fig. 12: : Pressure distribution on the X-31 A and pressure imprint onto the runway (Case II)

The second case (Case II) (figure 12) shows a very different surface pressure distribution, where the jet's foot print is much elongated and narrow when compared to the result of Case I in figure 10, since the jet is more aligned with the ground due to the lower angle of attitude. The foreplane, here set at a higher angle of incidence, also shows the typical pressure distribution of a more intense vortex breakdown. The major difference on the airplane in Case II can be found in the "wing mid position" of figure 13.
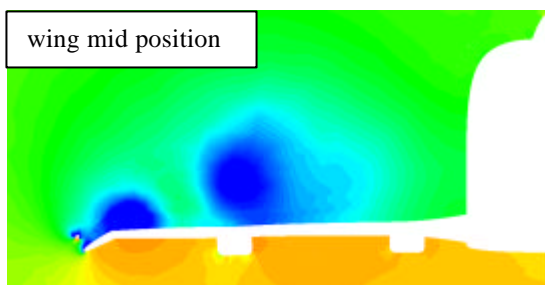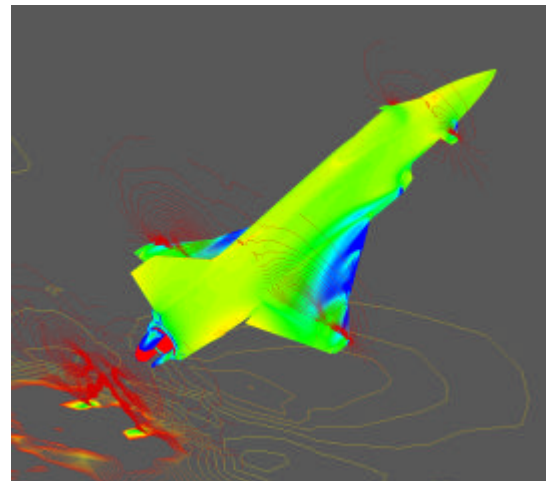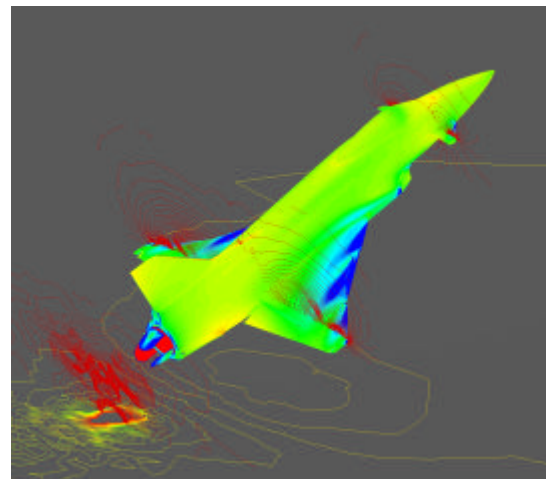

wing mid position

Fig. 13: Pressure around the X-31 A for Case II

Both wing vortices are much more stable due to the lower angle of attack imposed as well as by a favourable slat setting supporting their development. However the inboard system

indicates the burst phenomenon at this position in retarded axial velocities not shown here.

A: with ground

B: without ground

Fig. 14: X-31A at flow Case I with (A) and without (B) ground simulation

A comparison of the manoeuvre with and without ground effect at Case I conditions is shown in figure 14. While 14-A shows the ground effect, 14-B shows the pattern of an expanding jet cut by an inclined plane only. Figure 15 shows the result for Case II conditions.
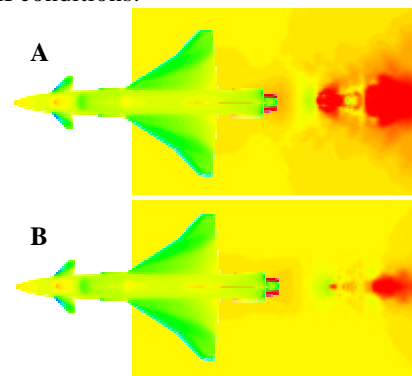

Fig. 15: X-31A at flow Case II with (A) and without (B) ground simulation

The very much widened pressure area at the far end of the fictitious ground plane of 15-B is due to the coarse mesh in this area remote of the aircraft.
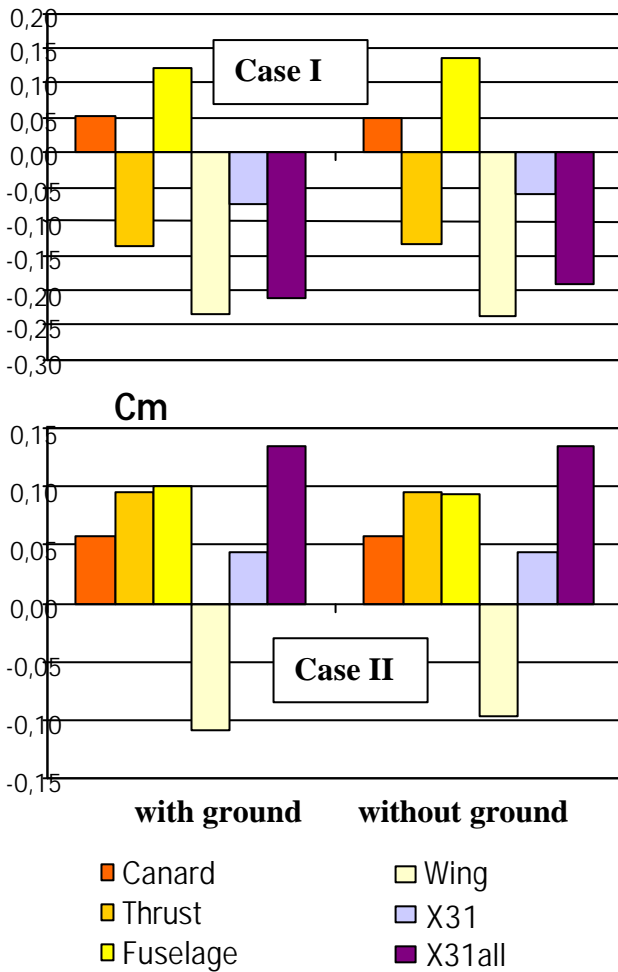

Fig. 16: Comparison of pitching moments with and without ground effect.

The comparison of the aerodynamic pitching moment of the steep descent positions with and without ground effect (fig. 16) shows a slight difference in the overall moment of the complete aircraft either including or excluding the aerodynamic effects of the air-intake and vector nozzle. In both cases the ground effect causes a tendency of pitch-down. The foreplane shows almost no difference in it's pitching moment contribution. At high angle of attack (Case I) the fuselage causes the primary pitch-down effect due to it's close proximity to the "air-cushion" caused by the aircraft's down-wash in between the aircraft and the ground. The nose high attitude of the aircraft exposes only the rear part of the fuselage to this pressure field (figs 8,10). Here also the thrust vector devices show a slight pitch-down tendency in ground effect. For Case II the wing is the primary pitch-down effect in ground effect (fig. 16). The Case II position brings the wing much closer to the ground which causes a wider footprint of the "air-cushion" (fig.12). This effect partially is countered by some suction at the rear end of the

fuselage (fig. 17) due to some local entrainment effects.

An evaluation of the upper fuselage and wing surfaces contribution to the pitching moments showed no differences. The small differences in the pressure distribution of Case I (fig. 14) did not result in pitch changes.
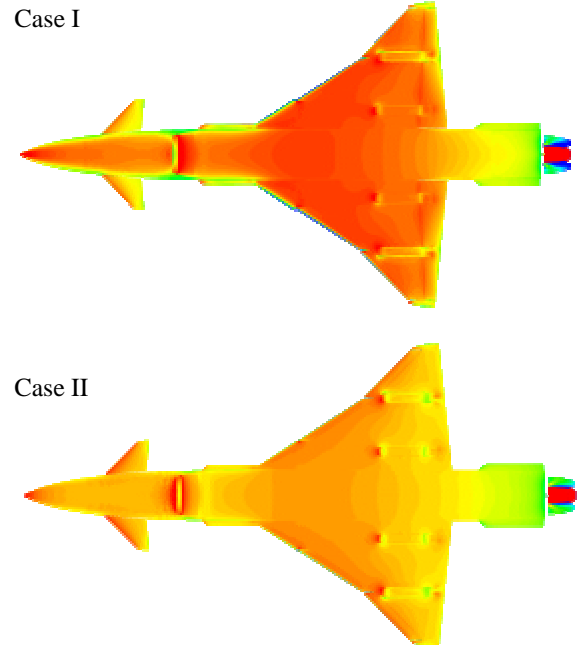
Case I

Case II

Fig. 17: Comparison of the bottom side pressure distribution of the X-31A at Case I and II in ground effect

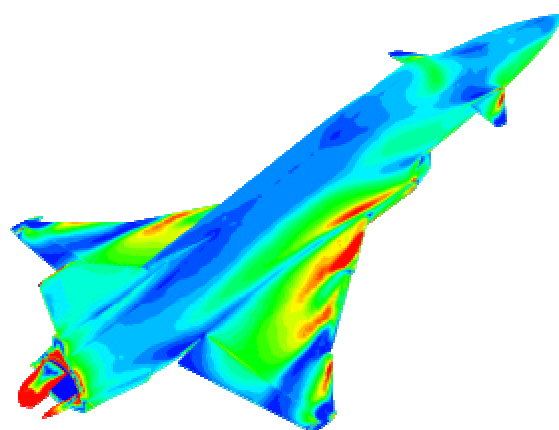The Case II results (fig. 15) showed no difference on the upper surface.

Fig. 18: Skin-friction pattern on the lee-ward side of the X-31A for Case I.

Figure 18 indicates the flow structure of the Case I result as already described in figure 10 and 11. The foot-print of the vortex-system can be traced very

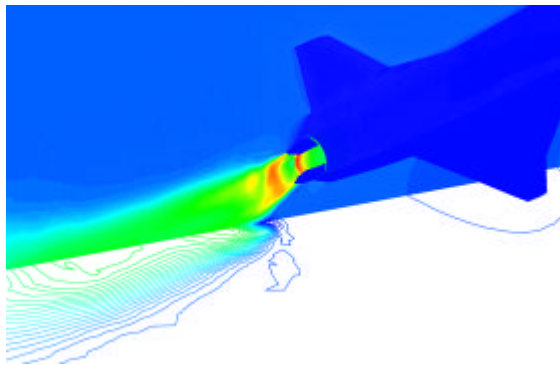well including the indications of vortex lift-off and burst.

Fig. 19: Jet in a Mach-distribution around the vector nozzle of the X-31A for the Case II steep descent manoeuvre.

The flow through the vector nozzle system can be seen in figure 19. Immediately aft of the internal nozzle duct the flow expands to supersonic flow, while in between the vector nozzle devices the flow is decelerated through a shock, only to be expanded again to supersonic speed aft of the vector system.

6   Unsteady, inviscid simulations

The simulation of the activated thrust vector system during a low speed (Mach = 0.17) pitch-up manoeuvre of the X-31A without ground was done by an Euler-simulation to reduce the computational effort. Here, the control surfaces were kept in neutral position. The engine boundary conditions simulated full thrust intake and nozzle conditions.

Figure 20 shows a part of the frame sequence of the manoeuvre with the pressure distribution on the surface. The first frame depicts the aircraft close to the beginning of the pitch-up motion with a pressure distribution typical for a fully developed vortex system both on the wing and the foreplane.

In the middle frame the trace of the vortex of the apex-strake ahead of the wing can be found along the side of the centre fuselage. The foreplane vortex is burst, while the wing vortex system also shows a strong pressure rise at almost wing mid position, indicating vortex breakdown there.

In the last frame, - the aircraft is exposed to high angle of attack - the vector devices have changed their setting in between the middle and the lower frame. This can be noticed by the distinct difference in the pressure pattern of the last frame when compared to the middle frame. Naturally the movie of the presentation shows this to a much better effect The computational mesh topology was kept unchanged during the manoeuvre, while the grid point motion was achieved through diffusion-equations with variable diffusion-coefficients,
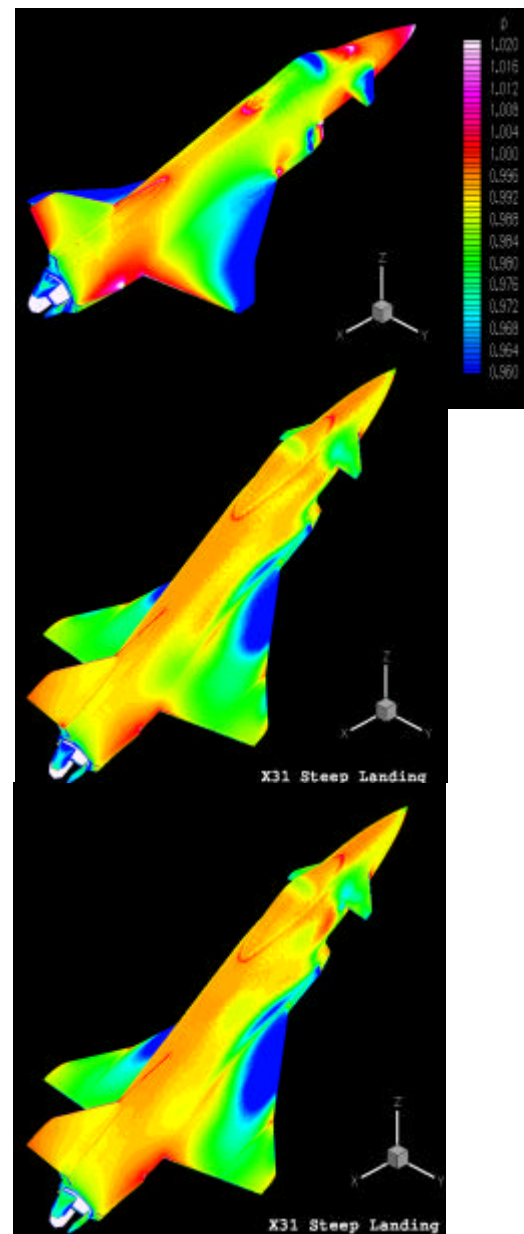

Fig. 20: X-31A pitch-up manoeuvre with simultaneous activation of the thrust vector devices, pressure distribution on frames of a movie.

weighted by the inverse size of the local cell volume. The ensueing set of linear equations was solved by a Galerkin-scheme for the decoupled geometric components x, y and z separately.

The control of the motions and the articulation of the control devices was sequenced through a simulation control tool. The results presented were achieved by the mere guidance of the configuration through a flight path copied from real time flight simulations or real flight test.

The aircraft together with it's computational domain is "moved" in the fixed geodetic frame of reference in the Lagrangian mode.

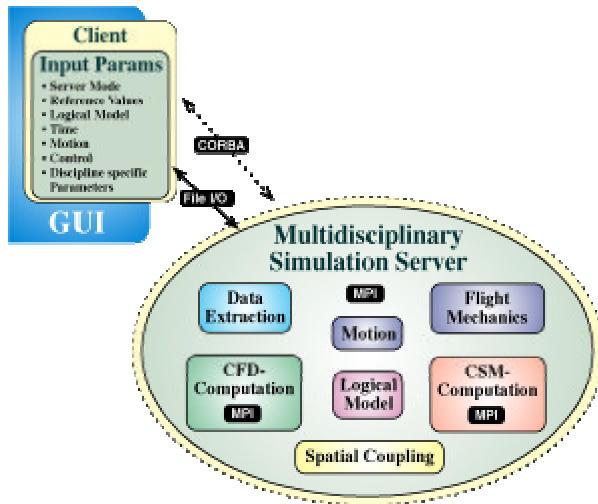For future applications the simultaneous evaluation of the forces and moments on the aircraft and it's

Fig. 21: General layout of a multidisciplinary simulation server environment

components can be extracted and used for the full simulation on the basis of the simulated aerodynamic flow field. This will include applied articulated controls and adjusted engine settings. Currently intense work is undertaken to allow for the proper geometric and computational grid adjustments necessary. The simulation control tool layout already holds the provisions for the geometric manipulations and local grid re-mesh operations.

Figure 21 gives a brief survey of this tool. Note the flight mechanics application and the provisions for CSM-computations to include aeroelastic effects. The logical model holds the information of the aircraft configuration and it's components including their kinematics. Since the CFD-computations and the numerical mesh operations are the most time consuming steps in an unsteady simulation with an aeroservo- or aeroservoelastic application in mind, the full process economically can be performed in a true parallel, distributed memory environment only.

Figure 22 shows the motion of the computational grid in three frames of a steep descent manoeuvre. The first frame shows the beginning of the motion. According to the manoeuvre the regime in between the aircraft and the ground in compressed. The last frame shows a significant distortion of some grid layers in between the ground the forward part of the aircraft. This effect could be countered by a modification of the basic mesh (the first frame) with a finer pre-processed grid in this area. A better approach would be a re-meshing of this area – a task being developed for the future. Unfortunately the Euler-simulation was delayed for the time of the paper and conference.
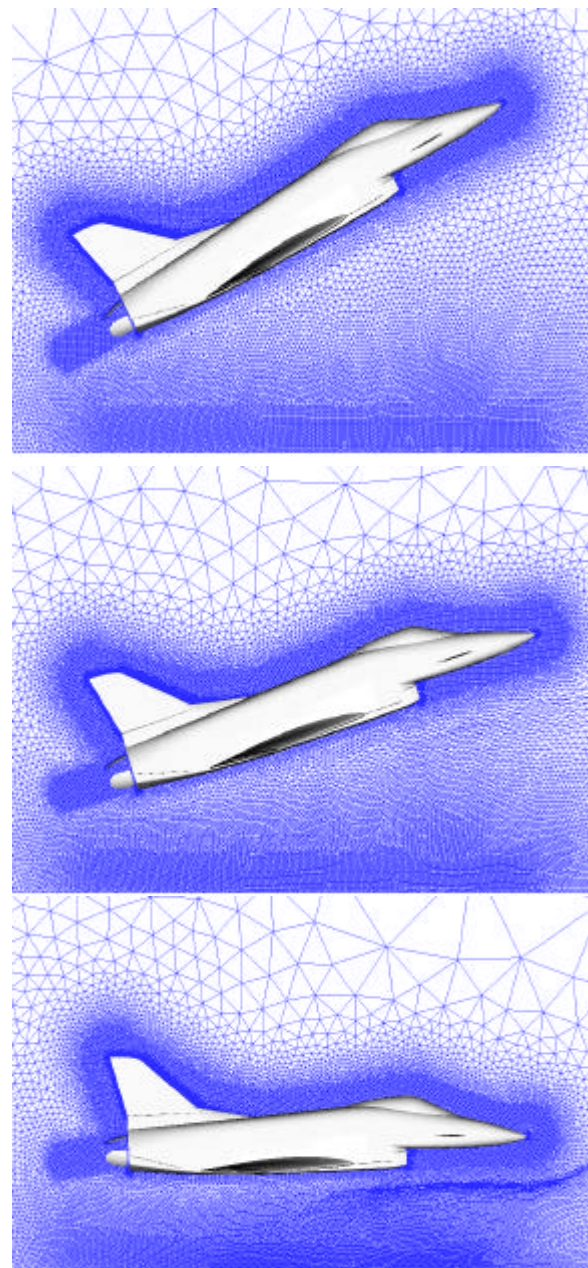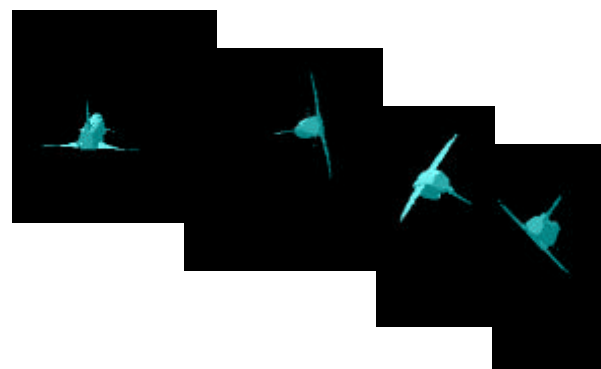

Fig. 22: X-31A mesh in the steep descent manoeuvre

Fig. 23: X-31A in a roll manoeuvre

As a simple substitute the Euler -simulation of a fast roll manoeuvre at Mach = 0.7 is shown here. Figure 23 depicts the manoeuvre as seen from a virtual chase-plane. Figure 24 shows selected frames of the simulation with the pressure distribution on the surface. Here the simplified X-31A model did not apply any controls and the thrust vector devices were deleted. The first frame shows the aircraft just at the beginning of the manoeuvre. It shows the pressure distribution typical for this low angle of attack. In the next frame the fast roll just reached 100^0 . The high roll rate causes a suction on the lower surface of the upward moving wing triggering a leading edge vortex at the outer wing panel. In the third frame at apprx. 180^0 the lower wing surface pressure distribution exhibits a fully developed vortex system. As can be seen from figure 23 a negative angle of attack is induced by the decent of the aircraft during the roll. The last frame shows the aircraft passing through almost 270^0 still showing the stagnation line on the leading edge of the wing before returning to a pressure pattern similar to the first frame after the completed roll.

7 Conclusion

The X-31A steep descent manoeuvres were investigated in steady state Navier-Stokes and unsteady Euler-simulations. The simulation was done with and without ground proximity together with the actuation of a thrust vector system and applied control surfaces. The geometry and the computational domain was discretized in unstructured meshes. The grid points were moved according to the motions, in which the configurations were guided by a multidisciplinary simulation server controlling the motions of the aircraft and evaluating the ensueing aerodynamic forces on the comp onents of the configuration. For all cases the results helped to understand complex flow structures of complex flight manoeuvres qualitatively. For future simulations moving controls such as flaps and slats are intended through the integration of moving geometries and the corresponding remeshing provisions.
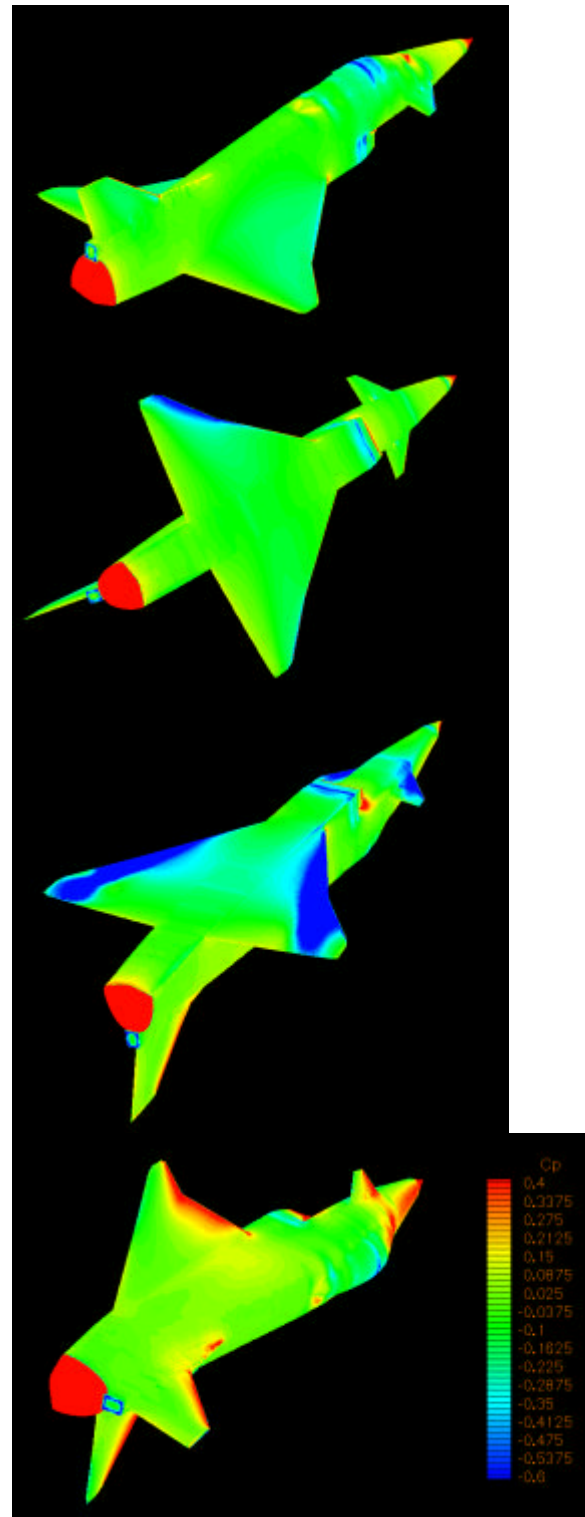

Fig. 24: Pressure on the X-31A during the roll manoeuvre of figure 23 in an Euler simulation

References

[1]   T. Gerold, O. Friedrich, J. Evans, M. Galle, *Calculation of Complex Three-Dimensional Configurations Employing the DLR-TAU-Code*, AIAA 97-0167, 1997

[2]   P. R. Spalart, S. R. Allmaras, *A one-equation turbulence model for aerodynamic flows,* La Recherche Aerospatiale, 1994, no 1, pp 5-21

[3]   D. Rowse, P. Thomas, L. Fornasier, A. Kamoulakos, *ESPRIT 25050 Julius*, Final Report July 2001

[4]   L. Fornasier, H. Rieger, U. Tremel, E. van der Weide, *Time-Dependent Aeroelastic Simulation of Rapid Manoeuvering Aircraft*, AIAA 2002-0949, Reno 2002

[5]   CentaurSoft, *Unstructured Meshgenerator Centaur*, www.centaursoft.com